Geostatistical characterisation of internal structure of mass-transport deposits from seismic reflection images and borehole logs

---

Please feel free to contact any of the authors, we welcome feedback:

Jonathan Ford (jford@inogs.it)
Angelo Camerlenghi (acamerlenghi@inogs.it)

Istituto Nazionale di Oceanografia e di Geofisica Sperimentale (OGS), Trieste, Italy

submitted to *Geophys. J. Int.*

Geostatistical characterisation of internal structure of mass-transport deposits from seismic reflection images and borehole logs

Jonathan Ford⋆, Angelo Camerlenghi

Istituto Nazionale di Oceanografia e di Geofisica Sperimentale (OGS), Trieste, Italy

July 2019

SUMMARY

Seismic reflection images of mass-transport deposits often show apparent chaotic, disordered or low-reflectivity internal seismic facies. The lack of laterally coherent reflections can prevent horizon-based interpretation of internal structure. This study instead inverts depth-domain seismic reflection images for geostatistical parameters describing the internal heterogeneity of mass-transport deposits by forward modelling their idealised spatial power spectra. If the internal heterogeneity approximates an anisotropic von Karman fractal medium these parameters can describe the structural fabric of the imaged mass-transport deposit. A Bayesian Monte Carlo Markov Chain inversion is performed to estimate posterior probability distributions for parameters representing the lateral and vertical dominant scale lengths and the Hurst number (roughness) of the P-wave velocity heterogeneity. The method is demonstrated on a synthetic multi-channel seismic reflection image and on a real data example from Nankai Trough, offshore Japan. To improve the discrimination between vertical and lateral dominant scale lengths, an estimate of the vertical dominant scale length from a nearby borehole is used as a prior in the inversion. The vertical and lateral dominant scale lengths are estimated with lower uncertainty when the borehole data is included; with the seismic image alone, only the aspect ratio of heterogeneity (ratio between the two dominant scale lengths) is reliably estimated.

Key words: submarine landslides – fractals and multifractals – statistical methods

1 INTRODUCTION

In recent years it has become increasingly common to acquire seismic reflection images of submarine mass-transport deposits (MTDs) (e.g., Berndt et al. 2012; Vanneste et al. 2014; Sun et al. 2017; Bellwald & Planke 2018). In addition, scientific drilling or coring is often performed to estimate geotechnical and petrophysical parameters, such as undrained shear strength and excess pore pressure (Camerlenghi et al. 2007; Strasser et al. 2011; Dugan 2012). A primary research goal of this data acquisition is to better quantify the geohazard potential from submarine mass-movement.

For traditional marine seismic reflection images of MTDs (dominant source frequency on the order of 50 Hz) internal reflectors often appear chaotic or disordered. This can prevent confident horizon-based interpretation of internal structure (Chopra & Marfurt 2016). An alternative approach to provide information on the internal structure is to characterise the geostatistics of heterogeneity within the medium.

The main goal of this study is to demonstrate a method to constrain the internal structural fabric of MTDs directly from reflection images. This is achieved by inverting for geostatistical parameters (lateral and vertical dominant scale lengths and Hurst number) under the assumption that the MTD can be approximated by an anisotropic von Karman fractal medium (after Irving & Holliger 2010). This approach is suitable even where the reflection image appears chaotic or disordered. A further goal is to demonstrate how to integrate geostatistical information from a vertical borehole log, where available, to better estimate lateral and vertical dominant scale lengths separately. The method is first validated on a synthetic model representing a typical submarine MTD scenario, with a modelled multi-channel

---

⋆ `jford@inogs.it`

seismic reflection image and a co-located synthetic vertical borehole. Then, the method is applied to a real data case study from the Nankai Trough, offshore Japan.

1.1 Previous work

There is a long history of using geostatistical techniques to characterise complex geology from geophysical data. This includes seismic imaging of the lower crust (Holliger & Levander 1992); investigating partial saturation in freshwater acquifers from ground-penetrating radar images (Irving et al. 2009); modelling random heterogeneities to characterise the seismic response of the crust and mantle at different scales (Carcione et al. 2005) and characterising complex turbidite systems from 3-D seismic reflection volumes (Caers et al. 2001). Some studies have explored the link between the spatial statistics of the geological medium and the power spectrum of the reflected wavefield. Irving & Holliger (2010) show an analytical relationship between band-limited, self-similar random media (generalised anisotropic von Karman random fractal media; Von Karman 1948) and a corresponding idealised reflection image. They demonstrate that it is possible to use this relationship to estimate geostatistical parameters characterising the P-wave velocity heterogeneity, such as the aspect ratio of lateral and vertical dominant scale lengths and the Hurst number (a self-similarity coefficient related to the roughness of the medium). This approach relies on the assumption that the reflection image approximates a so-called primary reflectivity section, an idealised seismic image. Irving et al. (2009) demonstrate that this technique can recover geostatistical parameters for zero-offset ground-penetrating radar images of shallow, partially saturated acquifers. Scholer et al. (2010) use a similar approach to estimate the correlation structure of P-wave velocity heterogeneity in the crystalline crust from seismic reflection images, including a term to compensate for the theoretical lateral resolution limit of migrated reflection images.

1.2 Internal structure of mass-transport deposits

Many internal structural fabrics for MTDs are documented in the literature. Ogata et al. (2014) report localised internal shear zones, slumping and intact blocks of included substrate in outcrop examples of exhumed fossil MTDs. Jackson (2011) observes internally coherent rafted megablocks emplaced within more chaotic sediments in an MTD imaged by a 3-D seismic reflection volume. These different internal fabrics reflect differing modes of slope failure, sediment properties and slide kinematics. Thus, improving our understanding of the internal structure of MTDs from geophysical data is vital to better constrain slope failure dynamics and to improve understanding of the geohazard potential from submarine slopes.

Core and borehole logs can give a high resolution 3-D reconstruction of strain fabric within MTDs (e.g., Strasser et al. 2011), but only for centimeter-scale structure at single point locations. Acoustic reflection techniques (e.g., multi-channel seismic and sub-bottom echosounder) are the only geophysical methods currently available to image the whole extent of submerged or buried MTDs in-situ, including headscarp, translational and toe domains. For this reason, acoustic reflection datasets are routinely acquired for the purpose of geohazard assessment.

2 METHODOLOGY

2.1 Geostatistics of internal heterogeneity

For this study we make the assumption that the small-scale P-wave velocity heterogeneity of MTDs approximates an anisotropic von Karman fractal medium (Von Karman 1948). We will characterise these apparently chaotic zones in terms of the following geostatistical parameters: the lateral and vertical dominant scale lengths, a_x and a_z, and the Hurst number, γ. The dominant scale lengths (also known as correlation lengths) a_x and a_z describe the upper limit of the self-similar part of a random medium. They control the degree of continuity of the medium in vertical and horizontal directions. For unfailed sediments, one would expect very long lateral dominant scale lengths due to the presence of laterally continuous beds.

After failure, sediments may become deformed due to shearing and disaggregation, reducing the lateral dominant scale length. Therefore the lateral dominant scale length is a useful structural parameter that can be a proxy for lateral shortening from deformation. The vertical dominant scale length is more closely related to the average thickness of beds, and therefore may be less affected by mass-transport. The Hurst number, $0 \leq \gamma \leq 1$, is a dimensionless parameter related to the degree of self-similarity, which controls the roughness or texture of the field. The Hurst number is related to the fractal dimension, D, by

$$D = N + 1 - \gamma \tag{1}$$

where N is the Euclidean dimension of the medium (Goff & Jordan 1988).

We can propose candidate models for the internal velocity structure of an MTD by generating parameterised geostatistical models. The relative likelihood of a proposed model can be estimated from the difference between the power spectrum of the observed seismic image and a forward modelled seismic image. This study will use an analytical relationship between the power spectrum of the medium and an idealised seismic image (from Irving & Holliger 2010) to efficiently forward model the power spectrum.

Setting this within a probabilistic inversion framework, we can suggest prior probability density functions (PDFs) for the model parameters, and compute posterior PDFs by sampling the model space using a Monte Carlo approach and estimating their likelihood. With proper sampling we can retrieve joint posterior PDFs for the model parameters. This gives an estimate of the most likely values for each parameter and an estimate of their respective uncertainties, for the observed data. In addition, *a priori* geological information can be incorporated when appropriate prior PDFs for the geostatistical parameters can be estimated.

Posterior estimates of such geostatistical parameters (with uncertainties) can constrain the possible internal structure of an MTD from the seismic image. This could be used to classify type of slope failure and discriminate between deformational domains (as in Gafeira et al. 2010). This also makes it possible to validate proposed outcrop analogues against a chaotic seismic image, where the geostatistical properties of the outcrop analogue can also be estimated.

Because the likelihood function is computed from the power spectrum, this framework can easily accommodate multiple geophysical observations (e.g., 2-D or 3-D depth-domain seismic images with 1-D borehole logs), so long as the power spectrum of the geophysical response can be related to the spatial power spectrum of the medium.

2.2 Stochastic random media

2.2.1 Spatial power spectra of stochastic media

A broad aim is to find a small number of parameters which can characterise the range of possible internal structure inside MTDs. For this study we generate stochastic models of MTDs defined by their 2-D spatial power spectra.

Here the velocity field, v, is represented by two components, a smoothly varying background component, v_0, and a zero-mean, small-scale stochastic component, v', such that

$$v(x,z) = v_0(x,z) + v'(x,z) \tag{2}$$

where $\frac{v'(x,z)}{v_0(x,z)} \ll 1$ (i.e., the stochastic component is small relative to the background). In general terms, the background velocity is that which is well resolved by geophysical techniques such as velocity tomography. At experimental bandwidths, however, the small-scale stochastic component generates the vast majority of observed reflections in a seismic image. The small-scale stochastic velocity structure is generally poorly resolved by seismic reflection experiments except perhaps by full-waveform modelling techniques, which can require significant acquisition effort, model conditioning and computational power, with little measure of uncertainty in the final result.

We make the assumption that the internal heterogeneity (small-scale stochastic structure, v_0) of an MTD can be approximated as a von Karman fractal medium. After Irving & Holliger (2010), the normalised 2-D spatial power spectrum of an anisotropic von Karman fractal medium is

$$P_{v'}(k_x, k_z) = \frac{c}{(k_x^2 a_x^2 + k_z^2 a_z^2 + 1)^{\gamma+1}} \tag{3}$$

where c is a normalising constant, a_x and a_z are the dominant lateral and vertical scale lengths and γ is the Hurst number.

2.2.2 Spatial power spectrum of an idealised seismic image

This study will follow the methodology presented in Irving & Holliger (2010) which links the random medium parameters to the 2-D power spectrum of a resulting idealised seismic image, sometimes referred to as a primary reflectivity section. The idealised seismic image is a convolutional, zero-offset, normal-incidence, constant density approximation. The formulation in depth-domain is as follows:

$$s(x, z) \approx r(x, z) * w(z) * h(x) \tag{4}$$

where $s(x, z)$ is the idealised seismic image in depth, $r(x, z)$ is the normal-incidence acoustic reflectivity, $w(z)$ is the source wavelet and $h(x)$ is a horizontal filter to account for the lateral resolution of a migrated seismic section (Scholer et al. 2010). Note that this idealised seismic image depends only on the P-wave velocity heterogeneity.

Assuming i) the only contribution to acoustic reflectivity is P-wave velocity heterogeneity; ii) reflections from the smooth background velocity (v_0) are negligible and iii) the source wavelet is stationary in depth within the analysis window, the idealised seismic response $s(x, z)$ depends only on the stochastic velocity component (v'):

$$s(x, z) \approx \frac{\delta v'(x, z)}{\delta z} * w(z) * h(x). \tag{5}$$

The spatial power spectrum of the stochastic component can then be related to the power spectrum of the seismic image by the Fourier transform:

$$P_s(k_x, k_z) = k_z^2 P_{v'}(k_x, k_z) \cdot P_w(k_z) \cdot P_h(k_x) \tag{6}$$

where P_w is the power spectrum of the source wavelet, w, and P_h is the power spectrum of the lateral resolution filter, h. It follows that the power spectrum of the seismic image can be directly related to the random medium parameters by Eq. 3:

$$P_s(k_x, k_z) = \frac{ck_z^2}{(k_x^2 a_x^2 + k_z^2 a_z^2 + 1)^{\gamma+1}} \cdot P_w(k_z) \cdot P_h(k_x) \tag{7}$$

Therefore it is possible to forward model an idealised spatial power spectrum which is comparable to a window of an observed seismic image under the following assumptions:

(i) The analysed window of the observed seismic image approximates a noise-free, zero-offset, true-amplitude, convolutional image in depth-domain.

(ii) The stochastic component of P-wave velocity heterogeneity (v') within the analysed window is an anisotropic von Karman fractal medium characterised by a_x, a_z and γ.

(iii) The geostatistical parameters and source wavelet are stationary over the analysed window.

Only physically realisable models are considered (i.e., dominant scale lengths are non-negative and non-zero).

2.3 Bayesian Monte Carlo Markov Chain inversion

This study uses a Bayesian Monte Carlo Markov Chain (MCMC) approach to obtain probabilistic estimates for each geostatistical parameter (Mosegaard & Tarantola 1995). This approach can invert for multiple parameters with arbitrary priors and unknown correlation between model parameters. Let $\mathbf{m}$ be a vector containing the model parameters and $\mathbf{d}_{obs}$ be a vector of observations. Bayes' Theorem states

$$P(\mathbf{m}|\mathbf{d}_{obs}) = \frac{P(\mathbf{d}_{obs}|\mathbf{m})P(\mathbf{m})}{P(\mathbf{d}_{obs})} \tag{8}$$

where $P(\mathbf{m}|\mathbf{d}_{obs})$ is the posterior probability density function (PDF), $P(\mathbf{d}_{obs}|\mathbf{m})$ is the likelihood function, $P(\mathbf{m})$ is the prior PDF for the model parameters and $P(\mathbf{d}_{obs})$ acts as a normalising constant. Thus

$$P(\mathbf{m}|\mathbf{d}_{obs}) \propto P(\mathbf{d}_{obs}|\mathbf{m})P(\mathbf{m}). \tag{9}$$

This relation allows us to link the the posterior probability density function (left) to the posterior probability distributions (right) obtained from the MCMC.

A requirement for probabilistic inversion is a suitable likelihood function — the probability that the proposed model parameters can reproduce the observed data, under some assumed observation and model errors. Here we use a simple likelihood function which assumes independent Gaussian errors (Mosegaard & Tarantola 1995):

$$P(\mathbf{d}_{obs}|\mathbf{m}) = \exp\left(-\frac{\|\mathbf{d}_{\mathbf{m}} - \mathbf{d}_{obs}\|^2}{2\sigma^2\|\mathbf{d}_{obs}\|^2}\right) \tag{10}$$

where $\mathbf{d}_{obs}$ and $\mathbf{d}_{\mathbf{m}}$ contain the power spectral density at each wavenumber pair (k_x, k_z) for the observed and modelled data, respectively. $\mathbf{d}_{\mathbf{m}}$ is obtained by forward modelling the power spectrum of the idealised seismic image for $\mathbf{m}$ using Eq. 7. If $\mathbf{d}_{\mathbf{m}} = \mathbf{d}_{obs}$ then the modelled data exactly match the observed data and the likelihood will equal 1 (i.e., $\mathbf{m}$ is the optimal model). σ is a precision parameter which is proportional to the standard deviation of the data noise and modelling errors. For the two scenarios presented in this study the σ parameter is selected by hand such that the MCMC converges (Mosegaard & Tarantola 1995).

Bayesian MCMC inversion samples the posterior PDF by a random walk through the model space. The Metropolis-Hastings criterion (Hastings 1970) is used to accept or reject new candidate models to the chain. To add a new element to the chain (i.e., a model $\mathbf{m}$ drawn from the prior PDFs), the likelihood is computed (Eq. 10). The acceptance ratio is the ratio of the likelihood of the proposed model and the likelihood of the previously accepted element of the chain. If the acceptance ratio is greater than 1 (i.e., the proposed model is more likely than the previously accepted one), the proposed model is automatically accepted to the chain. Otherwise, the proposed model is accepted with probability equal to the acceptance ratio. The output from an MCMC is an ensemble (chain) of accepted models. If the chain has converged (after a so-called “burn-in” period) the distribution of models in the ensemble will be proportional to the joint posterior PDF. The marginal distributions will be proportional to the marginal posterior PDFs for each parameter in the model. This allows estimates of most likely values and uncertainties for each parameter from histograms of the accepted models.

Irving & Holliger (2010) show that under typical experimental conditions, the two dominant scale length parameters a_x and a_z are strongly dependent on each other, such that it may be impossible to resolve each one individually from a reflection image alone. However, they show that is possible to reliably estimate the aspect ratio of heterogeneity $\alpha = \dfrac{a_x}{a_z}$. With an external estimate of one of the dominant scale lengths, for example a_z from a vertical borehole log, it should be possible to resolve a_x and a_z individually. For this study, the model parameters considered in the inversion are a_x, a_z and γ. Also presented in the results is a distribution representing $\alpha = \dfrac{a_x}{a_z}$. Bayesian approaches have the advantage of using prior PDFs, so prior geological information can be easily incorporated if it can be expressed in terms of the model parameters.

2.4 Workflow

2.4.1 Seismic reflection image inversion

The seismic reflection image should be true-amplitude migrated and in depth-domain. For the chosen chaotic window of the 2-D image (the MTD zone), the analysis proceeds as follows:

(i) Calculate the 2-D spatial power spectrum, $P_{obs}(k_x, k_z)$, of the chaotic window using a 2-D Fast Fourier Transform.

(ii) Estimate the power spectrum of the source, $P_w(k_z)$ (e.g., from the waterbottom reflection, for marine data) accounting for the average P-wave velocity within the analysis window.

(iii) Choose a suitable filter, $P_h(k_x)$, to represent the lateral resolution of the migrated reflection image. Often this is based on the dominant source wavelength. This study follows Scholer et al. (2010) in using a Gaussian low-pass filter with width proportional to the dominant wavelength. Clearly this approximation is only valid for source spectra that are approximately Gaussian, often the case for processed marine seismic reflection images. The filter parameters are chosen such that the amplitude of the Gaussian is 1% at half of the dominant wavelength, λ_{dom}:

$$h(x) = \exp\left(\frac{4x^2 \ln(0.01)}{\lambda_{\mathrm{dom}}^2}\right). \tag{11}$$

For each proposed model $\mathbf{m} = (a_x, a_z, \gamma)$:

(i) Forward model the idealised, zero-offset 2-D spatial power spectrum, $P_s(k_x, k_z)$ (Eq. 7).

(ii) Compute the likelihood of $P_s(k_x, k_z)$ with the non-negative, non-zero wavenumber components (Eq. 10).

(iii) Accept or reject the model to the Markov Chain according to the Metropolis-Hastings criterion (Section 2.3).

This procedure is repeated until the desired number of models have been accepted to the ensemble. The total MCMC sample size and length of inital samples to discard (the so-called "burn-in" period) are chosen by producing trace plots of each parameter for each MCMC experiment. For all experiments in this study the MCMCs for each parameter appear to converge to sampling the final posterior distributions after a maximum of several tens of samples, with low observed serial correlation between samples after convergence for chains of length 10000 samples. To ensure that none of the pre-convergence "burn-in" samples are included in the posterior distribution, the first 1000 samples of each MCMC are discarded from the final posterior distributions.

2.4.2 Vertical borehole log inversion

Because the probabilistic inversion approach uses prior PDFs as an input, we can alter these prior PDFs to reflect our *a priori* knowledge of the subsurface. For geohazard studies, for example, borehole logs and cores are often acquired to estimate geotechnical or petrophysical information about the MTD. As these logs have spatial power spectra, we can better constrain geostatistical parameters in the direction of the borehole.

Normally, boreholes are approximately vertical, so we can estimate a_z and γ independently from a vertical borehole log alone (e.g., Browaeys & Fomel 2009). The 1-D form of

Eq. 3 is

$$P_b(k_z) = \frac{ck_z^2}{(k_z^2 a_z^2 + 1)^{(\gamma+0.5)}} \tag{12}$$

where the exponent is modified for a field with Euclidean dimension 1 (Eq. 1). As borehole logs generally directly measure physical parameters we do not need to account for the effect of the source wavelet on the geophysical response of the medium.

Otherwise, the inversion proceeds as for the seismic reflection image.

3 RESULTS

3.1 Synthetic benchmark – buried submarine mass-transport deposit

This synthetic example is designed to benchmark the inversion for a typical marine geohazard survey. The data acquisition simulates a multi-channel, marine, towed-streamer acquisition over a chaotic MTD body buried under a water layer and heterogeneous sediment cover. The aim of this test is to estimate geostatistical parameters from the seismic reflection image with and without an *a priori* estimate of the vertical dominant scale length from a synthetic borehole velocity log.

The model is divided into two layers, a water layer and a sediment layer, both 350 m thick (see Fig. 1a). Background elastic parameters and geostatistical parameters for the small-scale stochastic component are given in Table 1. The sediment layer has linearly increasing background P- and S-wave velocity and includes a zone with significantly shorter lateral dominant scale length and distinct Hurst number to represent a buried, chaotic MTD. Otherwise, the MTD zone has the same background elastic parameters as the host sediment layer. The random medium zones are realised on a regular (staggered) 2-D mesh according to Ikelle et al. (1993).

This synthetic benchmark simulates a typical 2-D multi-channel marine acquisition geometry. Shot spacing is 40 m, with a zero-phase, 40 Hz Ricker source wavelet. The streamer is comprised of 25 receivers, at 20 m spacing with a near-offset of 20 m, giving a maximum offset of 500 m. For this synthetic test we use a pseudo-spectral, isotropic, visco-elastic scheme (Carcione et al. 2005; Carcione 2014) to forward model the seismic reflection response. The mesh is a staggered grid with regular grid spacing 2 m by 2 m. Sources and receivers are located in the first row of grid points ($z = 0$ m). The modelling timestep is 0.125 ms and the maximum time modelled is 1.1 s in order to record reflections from the deepest part of the model at the surface array. For this experiment, attenuation and free surface multiples are not considered. P- and S- wave quality factors are $Q_\mathrm{P} = Q_\mathrm{S} = 10000$ (i.e., negligible attenuation at seismic wavelengths) for all grid points; perfectly absorbing boundary conditions are imposed on all four boundaries of the mesh.

As the background velocity model is known and does not vary laterally, the seismic processing follows a basic marine imaging flow, with a pre-stack true-amplitude Kirchhoff time migration (to 60° maximum angle), outer angle mute (to eliminate refracted arrivals), stack and time-to-depth conversion using the background P-wave velocity model. The image is cut to the full-fold area, with maximum depth equal to the maximum depth in the synthetic model (Fig. 2a).

3.1.1 Borehole log inversion

The synthetic P-wave velocity borehole log is shown in Fig. 2b. The window analysed is the MTD zone between 500 m and 650 m depth. For the inversion, uniform priors are used: $0 < a_z \leq 75$ m (half of the window height) and $0 \leq \gamma \leq 1$. Marginal posterior probability distributions for a_z and γ are shown in Fig. 3a. Both parameters are centered closed to the true values (Table 2): the mean for a_z is 16.6 m (true value 20 m) and the mean for γ is 0.36 (true value 0.25).

3.1.2 Seismic image inversion

Two inversions were run on the seismic reflection image, with and without estimates of the vertical scale length a_z from the borehole. The synthetic seismic image is shown in Fig. 2a. The window analysed is the MTD zone highlighted in Fig. 1b.

For the first inversion (without constraint from a borehole), uniform priors are used.

$0 < a_x \leq 1500$ m, $0 < a_z \leq 75$ m and $0 \leq \gamma \leq 1$. Marginal posterior probability distributions for a_x, a_z and γ are shown in Fig. 3b, alongside a distribution representing $\alpha = \frac{a_x}{a_z}$. As predicted by Irving & Holliger (2010), a_x and a_z are individually poorly constrained and inaccurate (Table 2). The mean for a_x is 340 m (true value 160 m) and the mean for a_z is 38.3 m (true value 20 m). It should be noted that the standard deviations for both distributions are on the same order of magnitude as the mean values (222 m and 21.5 m respectively). The distribution of γ is also poorly constrained, with mean 0.23 (true value 0.25) and standard deviation 0.16. However, the distribution representing $\alpha = \frac{a_x}{a_z}$ is better constrained, with mean 8.6 (true value 8).

The second inversion is parameterised as the first, but includes a constraint for a_z and γ. The prior PDFs for a_z and γ are Gaussian, with mean and standard deviation from the results of the borehole-only inversion. The prior for a_x is uniform, as above: $0 < a_x \leq 1500$ m. The priors for a_z and γ are Gaussian: for a_z, mean $\mu = 16.61$ m and standard deviation $\sigma = 4.66$ m; for γ, $\mu = 0.36$ m and standard deviation $\sigma = 0.12$ m (Table 2). Marginal posterior probability distributions are shown in Fig. 3c.

With respect to the first inversion (seismic image only) the second inversion (seismic image with constraint from borehole) shows well-constrained marginal distributions for both a_x and a_z, with peaks close to their true values. This is in contrast to the first inversion, where a_x and a_z are poorly constrained with near-uniform marginal distributions. The distribution representing α has similar mean but is slightly better constrained. The marginal distribution for γ is also better constrained and centred on the true value.

3.2 Real data case study – Nankai Trough, offshore Japan

The Nankai Trough (offshore southwest Japan) is an oceanic trench formed by the subduction of the Philippine plate under the Eurasian plate. Associated accretion, seismicity and slope-steeping have resulted in significant mass-wasting during the last 3 Ma (Strasser et al. 2011). A large MTD is identified in a 3-D seismic volume (Fig. 4). Here we consider a 2-D profile extracted from the 3-D volume, chosen to show the maximum extent and thickness of the MTD. The body has a chaotic internal character, with little visible coherent structure.

The survey acquisition parameters are documented in Uraki et al. (2009). The sample interval in depth is 5 m, with a CDP spacing of approximately 18.75 m. The maximum observed thickness (at the point where the MTD intersects the edge of the seismic volume) is approximately 180 m (Strasser et al. 2011).

Also available are logging-while-drilling borehole logs from nearby International Ocean Discovery Programme (IODP) borehole C0018B (Henry et al. 2012), which penetrates the MTD (Fig. 4a). No sonic log was acquired, so the gamma ray log is used to estimate the vertical dominant scale length and Hurst number. Whilst the gamma ray log is not a measure of the P-wave velocity, it is sensitive to changes in lithology (specifically shale fraction), which should correlate with the P-wave velocity. It is expected that both gamma ray and sonic velocity logs should have similar geostatistics within a local interval of a 1-D borehole log.

3.2.1 Borehole log inversion

The gamma ray log from IODP borehole C0018B is shown in Fig. 4c. The analysis window is the MTD zone between 3235 m and 3295 m. For the inversion, uniform priors are used: $0 < a_z \leq 30$ m and $0 \leq \gamma \leq 1$. Marginal posterior probability distributions for a_z and γ are shown in Fig. 5a.

The marginal distribution for a_z has mean 5.21 m (standard deviation 1.22 m). The marginal distribution for γ has mean 0.41 (standard deviation 0.10) (Table 3).

3.2.2 Seismic image inversion

Two analysis windows are used on the seismic image (Fig. 4b). Both Zone A and Zone B have the same dimensions (1000 m by 60 m). Zone A is located downslope of Zone B, toward the toe of the MTD. Zone B is located relatively further upslope, in the more proximal middle part of the MTD. Two inversions are run for each zone, with and without estimates of the vertical scale length a_z and Hurst number γ from the borehole log.

For the first inversions (without constraint from a borehole), uniform priors are used: $0 < a_x \leq 350$ m, $0 < a_z \leq 35$ m and $0 \leq \gamma \leq 1$. Marginal posterior probability distributions for a_x, a_z and γ in both zones are shown in Fig. 5b, alongside a distribution representing $\alpha = \dfrac{a_x}{a_z}$.

The second inversions are parameterised as the first, but include a constraint from the borehole inversion results. The prior for a_x is uniform, as above: $0 < a_x \leq 350$ m. The priors for a_z and γ are Gaussian, fit to the marginal posterior probability distributions from the borehole-only inversion: for a_z, mean $\mu = 5.21$ m and standard deviation $\sigma = 1.22$ m; for γ, $\mu = 0.41$ m and standard deviation $\sigma = 0.13$ m (Table 3). Histograms of the final ensemble are shown in Fig. 5c.

With respect to the first inversion (seismic image only), the second inversion (seismic image with constraint from borehole) shows better-constrained marginal distributions for a_x, a_z and γ. This is in contrast to the first inversion, where a_x and a_z are poorly constrained with near-uniform marginal distributions. The marginal distributions for Zone A show a notably smaller mean a_x and α compared to Zone B, while maintaining similar distributions for a_z. The mean for γ decreases slightly from Zone A to Zone B.

4 DISCUSSION

This study applies a geostatistical inversion method (after Irving & Holliger 2010) to characterise the internal structure of MTDs from seismic reflection images, with and without a constraint from a vertical borehole log. We first demonstrate the method on a synthetic model representing a typical buried submarine MTD scenario and then on a real data case study from the Nankai Trough, offshore Japan. The method gives probabilistic estimates of lateral and vertical dominant scale lengths and the Hurst number of the internal heterogeneity. To the authors' knowledge, this is the first time that this technique has been validated for multi-channel, stacked seismic reflection data with a synthetic test. This is also the first published example demonstrating how to condition the inversion using priors derived from a vertical borehole log in order to better constrain the individual lateral and vertical dominant scale lengths. We suggest that this technique could be a useful tool to better constrain internal structure of MTDs as it can be applied even to chaotic seismic reflection images of MTDs, which are common but difficult to interpret using traditional horizon-based methods.

4.1 Synthetic inversion results

For the inversion performed on the synthetic seismic image with uniform priors, the estimated aspect ratio of heterogeneity, $\alpha = \frac{a_x}{a_z}$, is close to the true model value. However the individual lateral and vertical dominant scale lengths, a_x and a_z, and the Hurst number, γ, are poorly constrained (Fig. 3b). This result is expected from previous studies, which suggest that the 2-D power spectrum (equivalently the 2-D autocorrelation function) is most strongly sensitive to the aspect ratio of heterogeneity rather than to the individual dominant scale lengths or the Hurst number (Irving et al. 2009; Scholer et al. 2010; Irving & Holliger 2010).

The inversion is repeated using prior PDFs from estimates of a_z and γ from a synthetic borehole. Under the same inversion scheme, the individual lateral and vertical scale lengths and the Hurst number are better constrained and their marginal distributions are centred closer to the true values, compared to using uniform priors.

4.2 Nankai Trough case study inversion results

For the Nankai Trough experiment we consider two identically-sized data windows, Zone A and Zone B (Fig. 4b). Zone A is located towards the toe of the MTD. Zone B is located further upslope. The seismic character in both windows is chaotic, lacking laterally coherent seismic reflectors.

First, we invert for the geostatistical parameters in both windows with uniform priors (Fig. 5b). In Zone A, the aspect ratio of heterogeneity, α, is significantly smaller than in Zone B. Including priors for a_z and γ based on the nearby IODP borehole C0018B (Fig. 4c), we still see a reduction in α from Zone B to Zone A, but we see the distributions for lateral dominant scale length, a_x, are much better constrained.

MTDs often show extensional structures near the headwall, little deformation in the central translational zone and compressional structures in the toe region, where the flow may be confined (Fig. 6). The observed reduction in lateral dominant scale length from Zone B to Zone A is consistent with this interpretation of the MTD. More compression will result in increased stratal disruption, giving a shorter lateral dominant scale length compared to relatively undeformed sediments. This could explain the reduction in lateral dominant scale length and aspect ratio of heterogeneity.

The velocity heterogeneity within the MTD should be closely related to lithological heterogeneity. For mass-transport scenarios, this heterogeneity could be predominantly due to included megaclasts, intact blocks or intense folding from stratal disruption. For the Nankai Trough case study, we see a reduction in lateral dominant scale length and the aspect ratio of heterogeneity from Zone B to Zone A. This implies a reduction in the horizontal scale of the heterogeneity, possibly linked to increasing compression due to confinement at the toe of the slide. This reduction in lateral scale length is consistent with most conceptual models of the variation in internal structure from proximal to distal within the depositional part of mass-transport deposits (e.g., Bull et al. 2009, see Fig. 6).

4.3 Internal structure from geostatistical parameters

How should these geostatistical parameters be interpreted in the context of MTDs? These parameters are abstract and set in terms of a statistical model, not in terms of geological structure. We suggest that the dominant scale lengths can be proxies for relative deformation from both mass-transport processes and tectonic stresses. Increasing deformation (e.g., folding from compression, reduction in size of intact blocks due to progressive disaggregation) should reduce the lateral dominant scale length and also the aspect ratio of heterogeneity.

Here we only consider heterogeneity of the P-wave velocity field, as we believe this should capture much of the geological heterogeneity that controls the seismic response. In fact, this method could be used to describe any kind of geological heterogeneity, so long as it can be related to the acoustic impedance (the idealised seismic image approximation only models normal-incidence reflections). For the MTD case, for example, one could consider the MTD medium as a mixture of two component lithologies with distinct acoustic impedances (e.g., matrix and clasts). Thus estimating the geostatistical parameters can inform the geostatistics of the geology directly.

4.4 Limits in generalisation

Using a synthetic example we show that an idealised seismic image approximation (Section 2.2.2) is valid for one multi-channel marine seismic experiment, with a specific overburden and seismic character. This allows a computationally inexpensive inversion method (on the order of minutes on a standard desktop computer in 2019) to estimate random medium parameters from a window of a reflection image. The validity of the approximation will depend on the local geology and on the seismic imaging performed. Multiple scattering, attenuation and seismic noise will all reduce the validity of the idealised seismic image approximation.

The method presented in this study uses the spatial power spectrum to evaluate random media models and to estimate the misfit between a corresponding theoretical and observed seismic reflection image. For a given spatial power spectrum there exist infinite physical realisations of the corresponding random medium. It is important to note that this method only constrains the statistics of the heterogeneity, not the direct medium properties. It is possible that there are better representations, especially for small window sizes which may suffer from edge-effects from the Fast Fourier Transform. Some previous studies have used the autocorrelation function instead (Irving et al. 2009; Scholer et al. 2010).

This study only considers 2-D seismic profiles. Mass-transport is an inherently 3-D geological process, so strong lateral heterogeneity observed in the plane of the profile implies that strong heterogeneity perpendicular to the profile is also likely. This 3-D heterogeneity could generate strong out-of-plane reflections. For a chaotic seismic reflection image, it may be impossible to identify or remove these out-of-plane reflections during imaging or interpretation. It is presently unclear how the results of the inversion may be affected if these spurious reflections contaminate the analysis window.

Is the anisotropic von Karman random fractal medium a suitable statistical representation of the internal structure of MTDs? There exist many studies suggesting that geology in general has fractal-like properties (band-limited self-similarity; e.g., Goff & Jordan 1988; Turcotte 1997; Browaeys & Fomel 2009; Nelson et al. 2015). Analysis of MTDs in outcrop is necessary to determine if this could be a useful statistical model. The formulation used in this study (Eq. 3) assumes no dominant dip direction. This could be reasonable for MTDs deposited in the deep ocean, for example, but not if there has been post-depositional deformation from tectonics. In future work it should be straightforward to include dominant dip direction as an extra parameter in the inversion (see Yuan et al. 2014, for an example).

4.5 Future development

The technique compares seismic images in the power spectrum domain. This naturally allows integration of other geophysical data types which can be expressed in terms of their power spectra and of geological information as priors in the inversion. Ultimately, this technique should be able to integrate multiple geophysical and geological observations in a joint inversion. For the submarine MTD case, joint inversion of seismic, sub-bottom profiles and borehole logs could be a fruitful direction for geohazard research. Another direction for future work in this area is to apply this method to problems with higher dimensionality, such as 3-D seismic volumes and heterogeneity with a dominant dip direction.

5 CONCLUSIONS

We show that under certain assumptions it is possible to relate geostatistical parameters (lateral and vertical dominant scale lengths, Hurst number) of an anisotropic von Karman fractal medium to the 2-D power spectrum of the corresponding multi-channel seismic reflection image using Irving & Holliger (2010). We suggest that it is feasible to estimate such parameters from chaotic seismic reflection images of submarine MTDs to characterise their internal structure.

First we validate this technique on a synthetic scenario containing a buried chaotic body, representing a submarine MTD, imaged with a typical multi-channel marine seismic acquisition and penetrated by a synthetic borehole. Estimates of the aspect ratio of lateral and vertical dominant scale lengths from the seismic image agree well with the synthetic model. Previous studies have been unable to separate the individual lateral and vertical dominant scale lengths as the inversion is sensitive mainly to their aspect ratio (Irving & Holliger 2010). We estimate the vertical dominant scale length and Hurst number from the synthetic borehole log, and repeat the seismic inversion using these probabilistic estimates as Gaussian priors. The results including the constraint from the borehole show good agreement for individual lateral and vertical dominant scale lengths and Hurst number.

We then apply the technique to a real data case study from Nankai Trough, offshore Japan. The data considered are a seismic reflection profile and the gamma ray log from a borehole which penetrates a large MTD. Considering two analysis windows, one upslope and one downslope, we see a reduction in lateral dominant scale length towards the toe of the MTD. This is consistent with increasing deformation due to compression toward the toe of the slide.

Geostatistical inversion could be a useful tool to aid in constraining the internal structure of MTDs observed in seismic reflection data, even when they show an apparently chaotic internal seismic response. The geostatistical parameters considered in this study can be used to validate conceptual models of internal structure; as a proxy for varying strain or degree of deformation in different parts of the slide and to guide future data acquisition to better image internal structure. We have shown that it is possible to estimate the lateral and vertical dominant scale lengths separately with an external estimate of vertical dominant scale length, such as from a vertical borehole log. The lateral dominant scale length (alternatively the aspect ratio of heterogeneity) in particular could be a good proxy for the extent of sediment deformation and stratal disruption within an MTD.

ACKNOWLEDGMENTS

Jonathan Ford was supported by a Marie Curie Doctoral Fellowship through the SLATE Innovative Training Network within the European Union Framework Programme for Research and Innovation Horizon 2020 under Grant Agreement No. 721403. The Kumano 3-D seismic dataset was provided by Greg Moore (SOEST). Seismic processing and imaging was performed using Seismic Un*x (Cohen & Stockwell 2016). Thanks to Philippe Cance and Davide Gei for providing the pseudo-spectral numerical modelling code and for discussion on the topic. The quality of this manuscript was greatly improved thanks to constructive reviews from Umberta Tinavella, José Carcione and Aldo Vesnaver.

REFERENCES

Bellwald, B. & Planke, S., 2018. Shear margin moraine, mass transport deposits and soft beds revealed by high-resolution P-Cable three-dimensional seismic data in the Hoop area, Barents Sea, *Geological Society, London, Special Publications*, p. SP477.29.

Berndt, C., Costa, S., Canals, M., Camerlenghi, A., de Mol, B., & Saunders, M., 2012. Repeated slope failure linked to fluid migration: The Ana submarine landslide complex, Eivissa Channel, Western Mediterranean Sea, *Earth and Planetary Science Letters*, **319-320**, 65–74.

Browaeys, T. J. & Fomel, S., 2009. Fractal heterogeneities in sonic logs and low-frequency scattering attenuation, *Geophysics*, **74**(2), WA77–WA92.

Bull, S., Cartwright, J., & Huuse, M., 2009. A review of kinematic indicators from mass-transport complexes using 3D seismic data, *Marine and Petroleum Geology*, **26**(7), 1132–1151.

Caers, J., Avseth, P., & Mukerji, T., 2001. Geostatistical integration of rock physics, seismic amplitudes, and geologic models in North Sea turbidite systems, *The Leading Edge*, **20**(3), 308–312.

Camerlenghi, A., Urgeles, R., Ercilla, G., & Brückmann, W., 2007. Scientific ocean drilling behind the assessment of geo-hazards from submarine slides, *Scientific Drilling*, **4**, 45–47.

Carcione, J. M., 2014. *Wave Fields in Real Media: Wave Propagation in Anisotropic, Anelastic, Porous and Electromagnetic Media*, vol. 38, Elsevier.

Carcione, J. M., Finetti, I. R., & Gei, D., 2005. Seismic modelling applied to interpretation of a CROP crustal section in the Adriatic Sea, in *CROP Project: Deep Seismic Exploration of the Central Mediterranean and Italy*, vol. 1, p. 794, ed. Finetti, I. R., Elsevier.

Chopra, S. & Marfurt, K., 2016. Understanding the seismic disorder attribute and its applications, *The Leading Edge*, **35**(8), 695–702.

Cohen, J. K. & Stockwell, J. J. W., 2016. CWP/SU: Seismic Un*x Release No. 44R2: an open source software package for seismic research and processing, *Center for Wave Phenomena, Colorado School of Mines.*

Dugan, B., 2012. Petrophysical and consolidation behavior of mass transport deposits from the northern Gulf of Mexico, IODP Expedition 308, *Marine Geology*, **315-318**, 98–107.

Gafeira, J., Long, D., Scrutton, R., & Evans, D., 2010. 3D seismic evidence of internal structure within Tampen Slide deposits on the North Sea Fan: are chaotic deposits that chaotic?, *Journal of the Geological Society*, **167**(3), 605–616.

Goff, J. A. & Jordan, T. H., 1988. Stochastic Modeling of Seafloor Morphology: Inversion of Sea Beam Data for Second-Order Statistics, *Journal of Geophysical Research: Solid Earth*, **93**(B11), 13589–13608.

Hastings, W. K., 1970. Monte Carlo sampling methods using Markov chains and their applications, *Biometrika*, **57**(1), 97–109.

Henry, P., Kanamatsu, T., Moe, K., & the Expedition 333 Scientists, 2012. Proceedings of the Integrated Ocean Drilling Program Volume 333 Expedition Reports - NanTroSEIZE Stage 2: Subduction Inputs 2 and Heat Flow, **333**, 16.

Holliger, K. & Levander, A. R., 1992. A stochastic view of lower crustal fabric based on evidence from the Ivrea Zone, *Geophysical Research Letters*, **19**(11), 1153–1156.

Ikelle, L. T., Yung, S. K., & Daube, F., 1993. 2-D random media with ellipsoidal autocorrelation functions, *Geophysics*, **58**(9), 1359–1372.

Irving, J. & Holliger, K., 2010. Geostatistical inversion of seismic and ground-penetrating radar reflection images: What can we actually resolve?, *Geophysical Research Letters*, **37**(21).

Irving, J., Knight, R., & Holliger, K., 2009. Estimation of the lateral correlation structure of subsurface water content from surface-based ground-penetrating radar reflection images, *Water Resources Research*, **45**(12).

Jackson, C., 2011. Three-dimensional seismic analysis of megaclast deformation within a mass transport deposit; Implications for debris flow kinematics, *Geology*, **39**, 203–206.

Mosegaard, K. & Tarantola, A., 1995. Monte Carlo sampling of solutions to inverse problems, *Journal of Geophysical Research: Solid Earth*, **100**(B7), 12431–12447.

Nelson, C. E., Hobbs, R. W., & Rusch, R., 2015. On the Use of Fractal Surfaces to Understand Seismic Wave Propagation in Layered Basalt Sequences, *Pure and Applied Geophysics*, **172**(7), 1879–1892.

Ogata, K., Pogačnik, Ž., Pini, G. A., Tunis, G., Festa, A., Camerlenghi, A., & Rebesco, M., 2014.

The carbonate mass transport deposits of the Paleogene Friuli Basin (Italy/Slovenia): Internal anatomy and inferred genetic processes, *Marine Geology*, **356**, 88–110.

Scholer, M., Irving, J., & Holliger, K., 2010. Estimation of the correlation structure of crustal velocity heterogeneity from seismic reflection data, *Geophysical Journal International*, **183**(3), 1408–1428.

Strasser, M., Moore, G. F., Kimura, G., Kopf, A. J., Underwood, M. B., Guo, J., & Screaton, E. J., 2011. Slumping and mass transport deposition in the Nankai fore arc: Evidence from IODP drilling and 3-D reflection seismic data, *Geochemistry, Geophysics, Geosystems*, **12**(5), Q0AD13.

Sun, Q., Alves, T., Xie, X., He, J., Li, W., & Ni, X., 2017. Free gas accumulations in basal shear zones of mass-transport deposits (Pearl River Mouth Basin, South China Sea): An important geohazard on continental slope basins, *Marine and Petroleum Geology*, **81**(Supplement C), 17–32.

Turcotte, D. L., 1997. *Fractals and chaos in geology and geophysics*, Cambridge University Press.

Uraki, S., Kido, Y., Sanada, Y., Kuramoto, S., Okano, T., Saga, H., Park, J., Moore, G., & Taira, A., 2009. Kumano-nada 3D seismic data acquisition and processing, *Butsuri Tansa*, **62**, 277–288.

Vanneste, M., Sultan, N., Garziglia, S., Forsberg, C. F., & L'Heureux, J.-S., 2014. Seafloor instabilities and sediment deformation processes: The need for integrated, multi-disciplinary investigations, *Marine Geology*, **352**, 183–214.

Von Karman, T., 1948. Progress in the Statistical Theory of Turbulence, *Proceedings of the National Academy of Sciences of the United States of America*, **34**(11), 530–539.

Yuan, G., Pei-Min, Z. H. U., Hui, L. I., & Xiao-Yong, L. I., 2014. Estimation of 2d Stationary Random Medium Parameters from Post-Stack Seismic Data, *Chinese Journal of Geophysics*, **57**(4), 450–461.

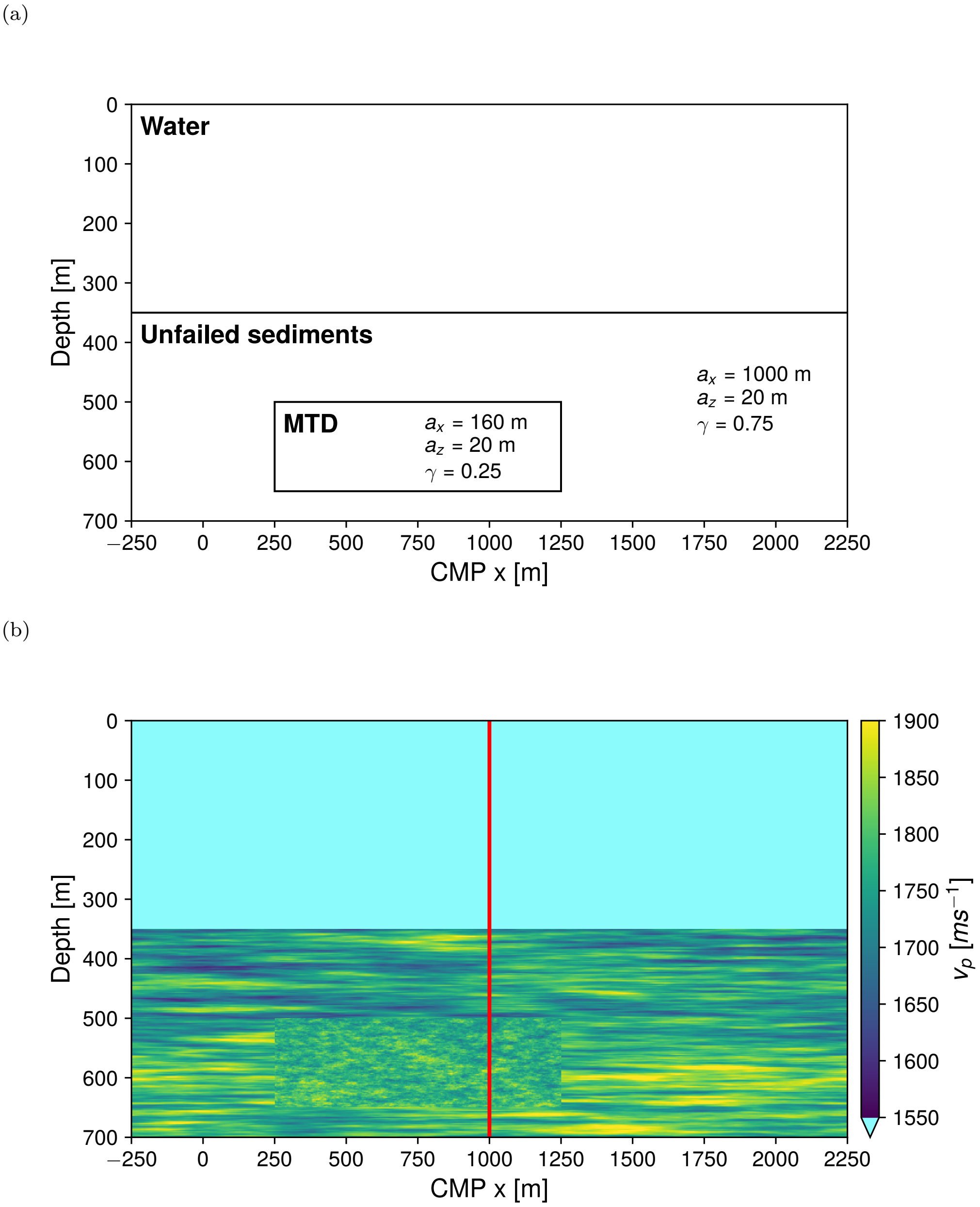

Figure 1. Synthetic buried mass-transport deposit model. a) Geostatistical parameters: lateral and vertical scale lengths (a_x and a_z) and Hurst number (γ) for each model zone. The water layer is uniform. Background elastic parameters are given in Table 1. b) P-wave velocity model. The location of the synthetic borehole is shown in solid red.

(a)

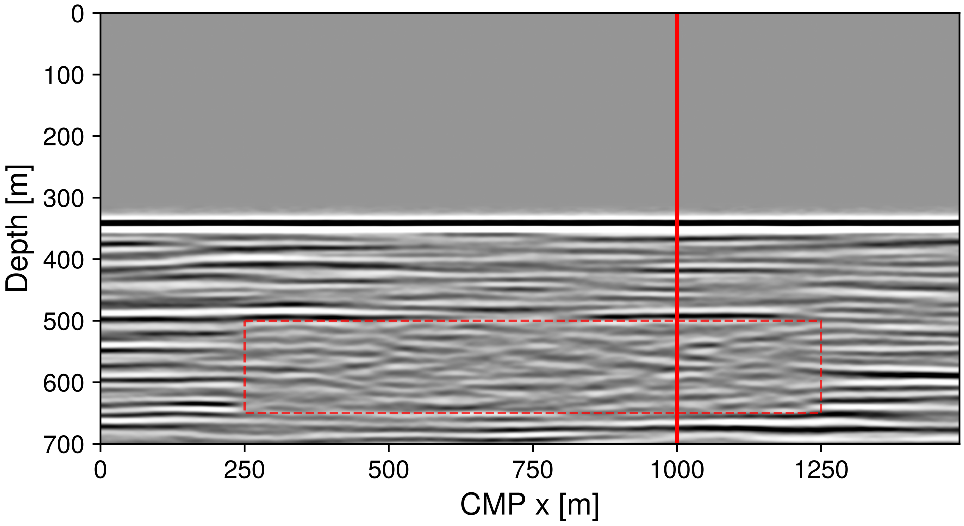

(b)

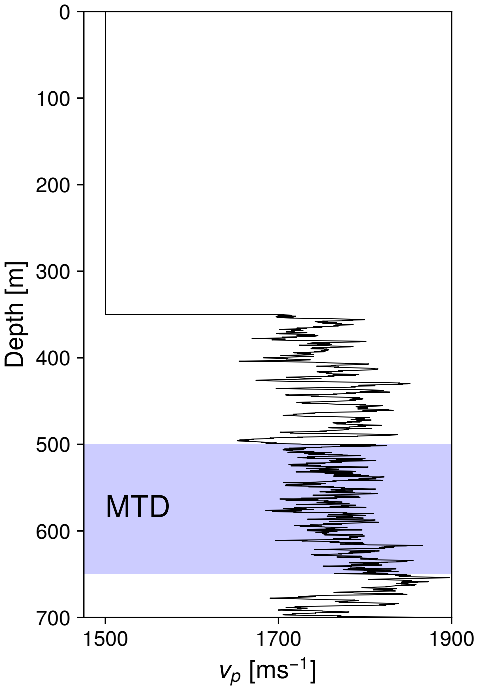

Figure 2. Synthetic buried mass-transport deposit modelling results. a) Seismic reflection image in depth-domain (pre-stack time migrated and converted to depth using the smooth background P-wave velocity function in Table 1). Location of the synthetic borehole is shown in solid red. The mass-transport deposit zone (dashed red) shows a more disordered, chaotic seismic character compared to the more stratified overburden sediments. b) P-wave velocity log sampled at 0.25 m.

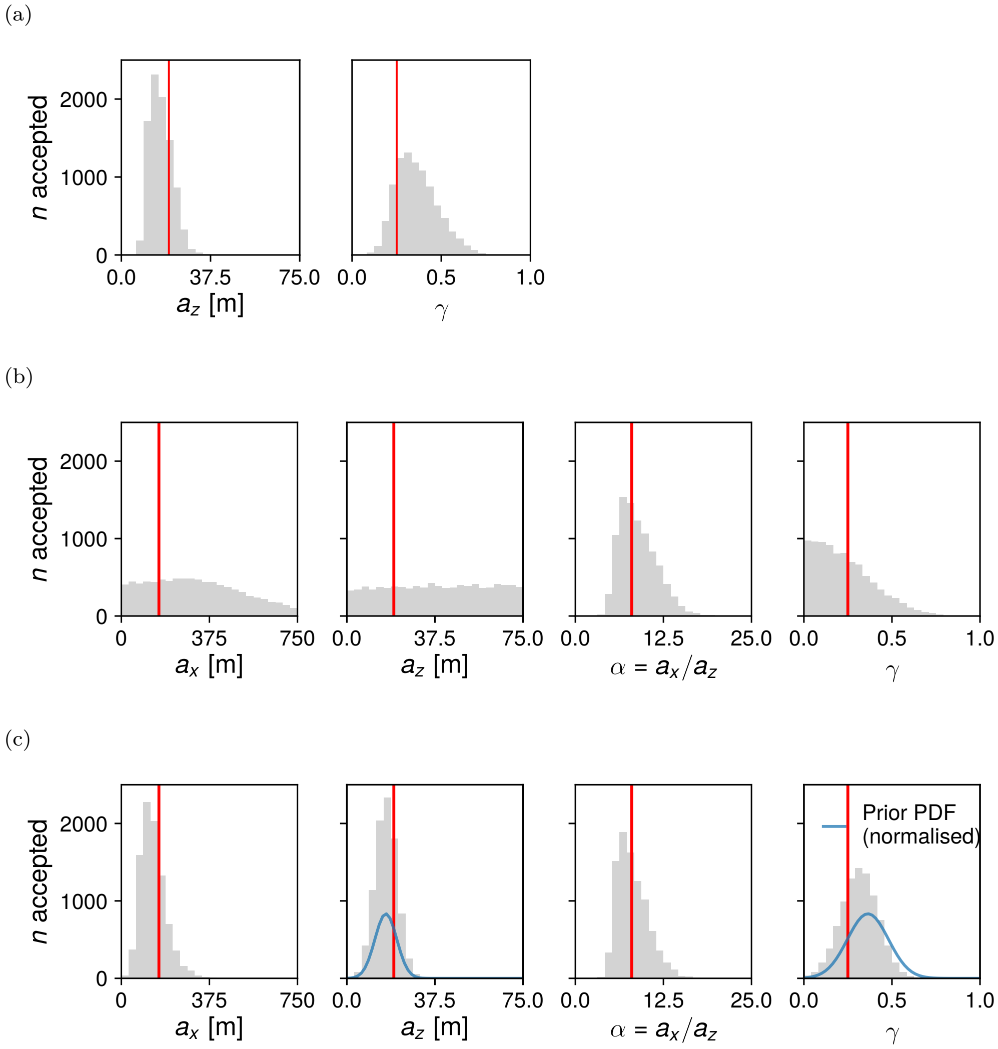

Figure 3. Marginal posterior probability distributions for the synthetic buried mass-transport deposit benchmark for dominant lateral and vertical scale lengths, a_x and a_z, aspect ratio of heterogeneity, $\alpha = \dfrac{a_x}{a_z}$, and Hurst number, γ. True values are shown in red. Details of priors are given in the text. a) P-wave velocity log from the synthetic borehole. b) Seismic image (Fig. 2a). c) Seismic image (Fig. 2a) with constraints on a_z and γ from the synthetic borehole log.

(a)

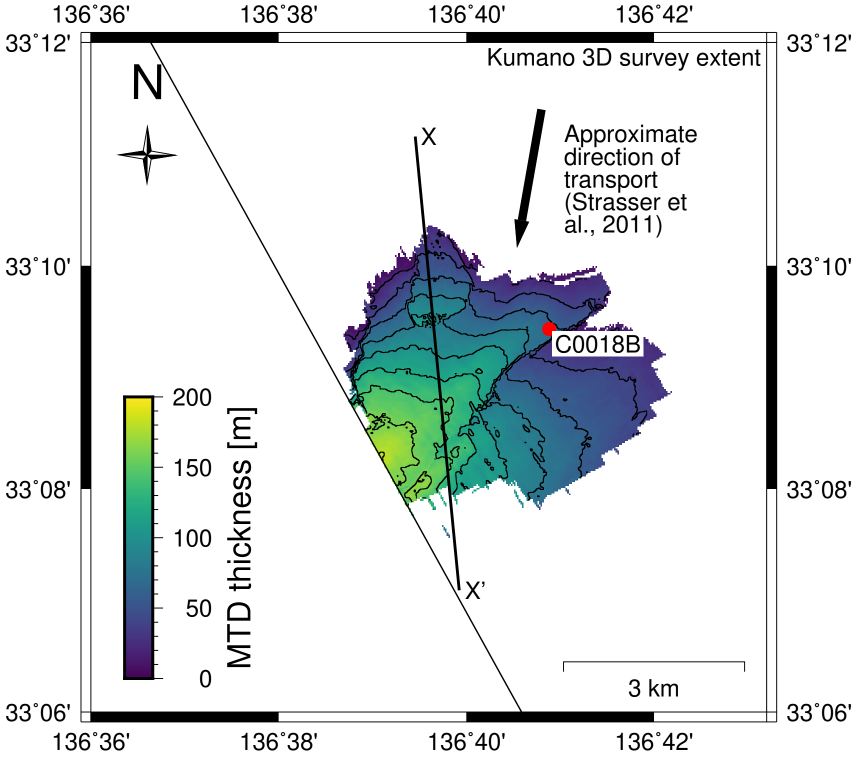

(b)

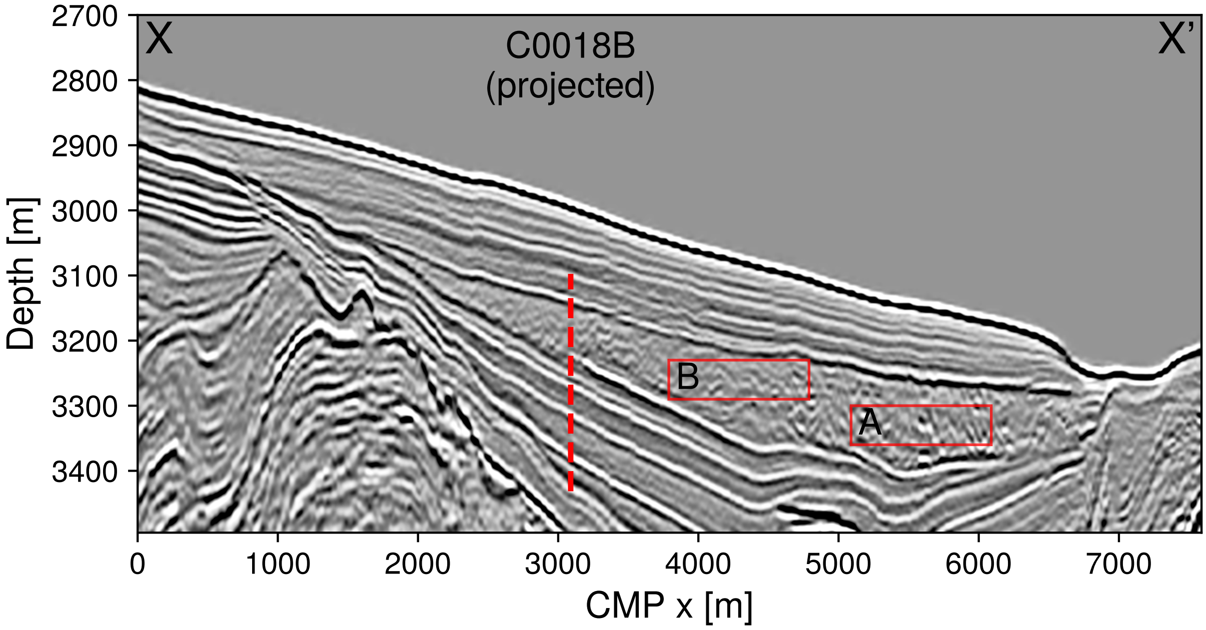

Figure 4. Nankai Trough case study data. a) Map showing extent of the Kumano 3-D seismic volume, the thickness of the mass-transport deposit, profile X-X' and IODP borehole C0018B. b) Seismic reflection profile X-X' (from the 3-D volume) showing a buried mass-transport deposit. The body lacks laterally coherent internal reflections compared to the unfailed sediments surrounding it. Zones A and B are indicated alongside the extent of the IODP borehole C0018B (dashed red line; Fig. 4c) when projected onto the profile. c) Logging-while-drilling gamma ray log from IODP borehole C0018B (downsampled to 0.25 m).

(c)

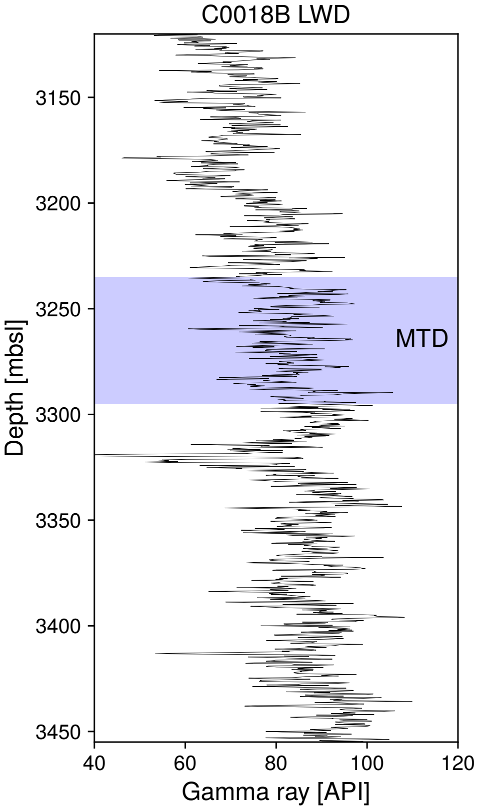

Figure 4. (continued)

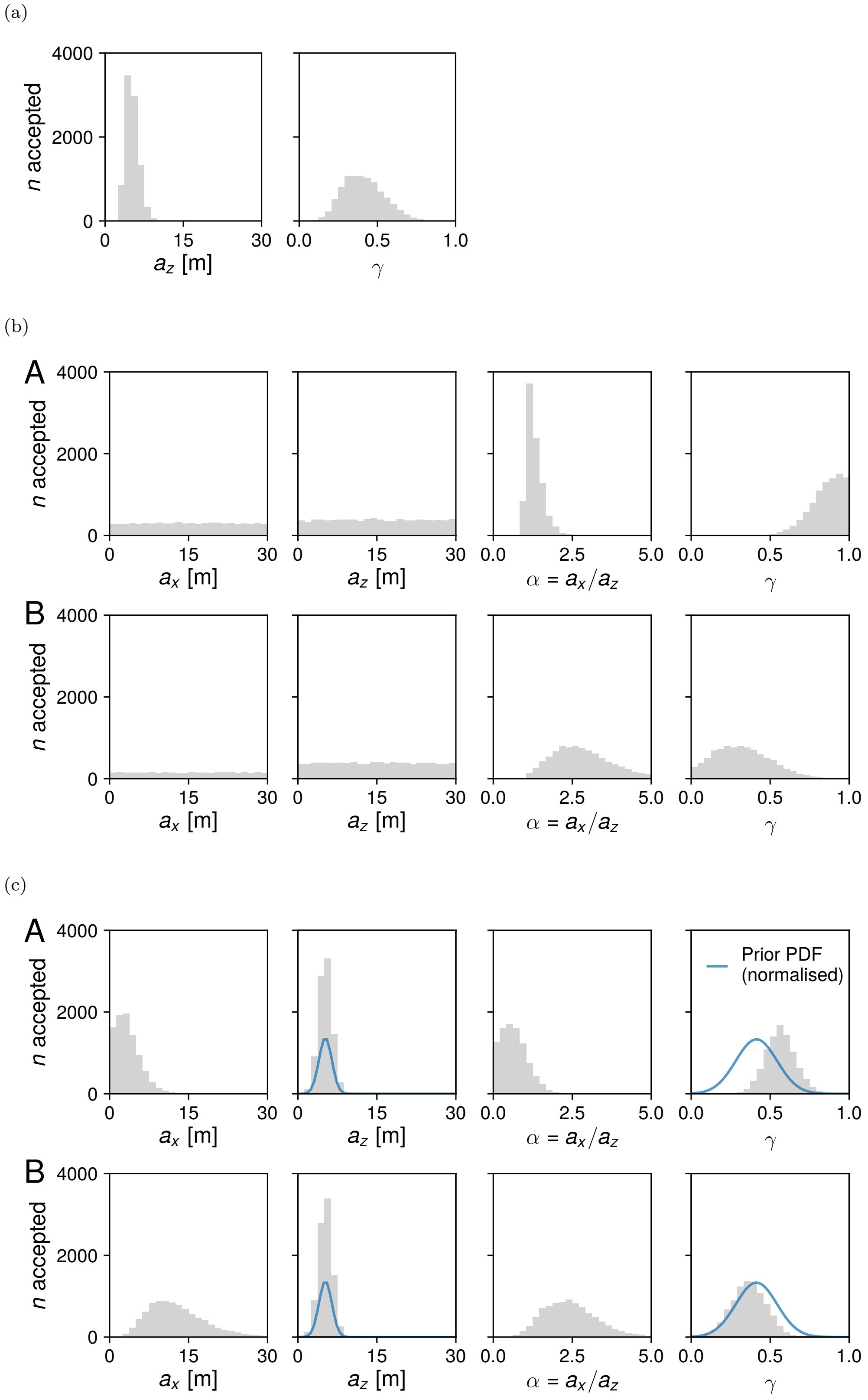

Figure 5. Marginal posterior probability distributions for the Nankai Trough case study for dominant lateral and vertical scale lengths a_x and a_z, aspect ratio of heterogeneity $\alpha = \frac{a_x}{a_z}$, and Hurst number γ. See text for details of priors. a) MTD zone of the gamma ray log from IODP borehole C0018B. b) Zones A (downslope) and B (upslope) of the seismic profile (Fig. 4b). c) Zones A (downslope) and B (upslope) of the seismic profile (Fig. 4b) with a constraint on a_z and γ from the borehole log.

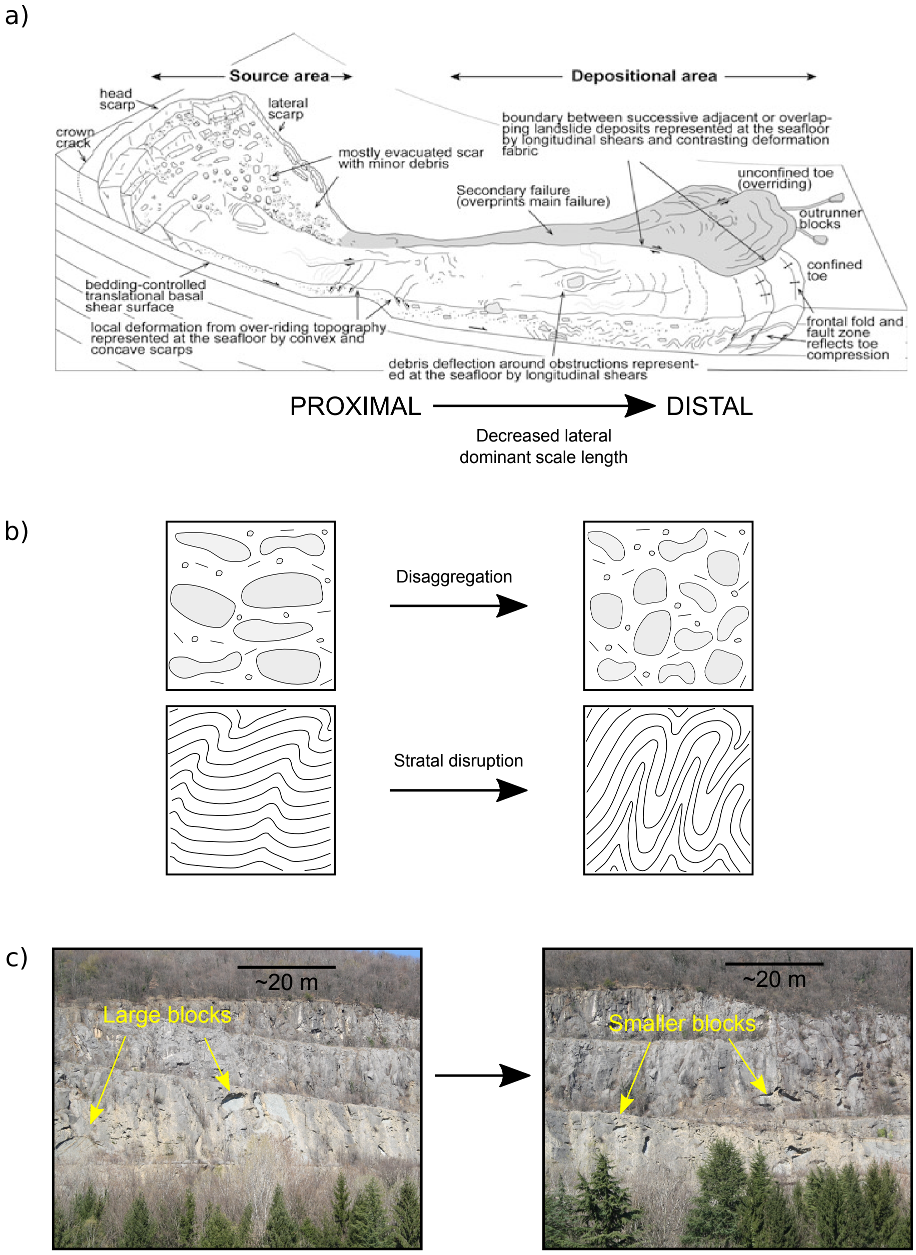

Figure 6. a) Schematic diagram showing representative internal structure found within submarine landslides and mass-transport deposits (from Bull et al. 2009). Note increasing deformation due to confinement towards the toe of the slide. b) Illustration of two mechanisms for reducing the lateral dominant scale length by mass-transport – disaggregation of large coherent intact blocks and stratal disruption of soft sediments. In general increased deformation will result in a decrease in lateral dominant scale length (and aspect ratio of heterogeneity). c) Outcrop example of variation in lateral dominant scale length due to a reduction in size of included megaclasts (Vernasso Quarry, NE Italy).

Table 1. Background elastic parameters and geostatistical parameters for each unit in the synthetic model (Fig. 1). z is the depth below the waterbottom, v_P and v_S are the P- and S-wave velocities, respectively, and ρ is the density.

	Background elastic parameters (v_0)			Geostatistical parameters (v')		
	$v_\mathrm{P}(z)$ [m s $^{-1}$]	$v_\mathrm{S}(z)$ [m s $^{-1}$]	ρ [kg m $^{-3}$]	a_x [m]	a_z [m]	γ []
Water	1500	—	1000	—	—	—
Sediment	$1750 + 0.3z$	$875 + 0.15z$	1600	1200	20	0.75
MTD	$1750 + 0.3z$	$875 + 0.15z$	1600	160	20	0.25

Table 2. Summary statistics for the synthetic benchmark marginal posterior probability distributions for dominant lateral and vertical scale lengths, a_x and a_z, aspect ratio of heterogeneity $\alpha = \frac{a_x}{a_z}$, and Hurst number γ. Mean, μ, and standard deviation, σ for each marginal distribution are shown.

	Mean, μ				Standard deviation, σ			
Experiment	a_x [m]	a_z [m]	$\alpha = \frac{a_x}{a_z}$	γ	a_x [m]	a_z [m]	$\alpha = \frac{a_x}{a_z}$	γ
Synthetic model (true values)	**160**	**20**	**8**	**0.25**	—	—	—	—
Synthetic borehole	—	16.6	—	0.36	—	4.7	—	0.12
Seismic image	340	38.3	8.9	0.23	222	21.5	2.6	0.16
Seismic image (with borehole)	136	16.7	8.1	0.32	54	4.6	2.2	0.10

Table 3. Summary statistics for the Nankai Trough case study marginal posterior probability distributions for dominant lateral and vertical scale lengths, a_x and a_z, aspect ratio of heterogeneity, α, and Hurst number, γ. Mean, μ, and standard deviation, σ for each marginal distribution are shown.

	Mean, μ				Standard deviation, σ			
Experiment	a_x [m]	a_z [m]	$\alpha = \frac{a_x}{a_z}$	γ	a_x [m]	a_z [m]	$\alpha = \frac{a_x}{a_z}$	γ
Borehole C0018B	—	5.21	—	0.41	—	1.22	—	0.13
Zone A	19.68	15.06	1.30	0.85	12.08	8.62	0.25	0.10
Zone A (with borehole)	3.46	5.22	0.66	0.57	2.39	1.23	0.42	0.09
Zone B	43.54	14.95	2.90	0.32	31.01	8.59	1.07	0.17
Zone B (with borehole)	12.85	5.22	2.46	0.37	5.65	1.23	0.89	0.11